Effects of partially stabilized zirconia fueled with Borassus biofuel at different piston bowl geometries in LHR engine

C. Sakthi Rajan[1] · K. Muralidharan[2]

Abstract

The current computational fluid dynamics (CFD) speculate reveals piston bowl geometry's impact on an immediate base engine execution and discharge. Different bowl shapes, that is, shallow combustion chamber, hemispheric combustion chamber, and toroidal combustion chamber (TCC), were made with a reference compression ratio of 17.5:1. ANSYS V18.1 was used for numerical investigation, in tandem with the wise burning model. It was clearly identified that TCC cylinder bowl geometry delivered the proper air–fuel mixing blend inside the cylinder chamber, which prompts a homogeneous charge. Further, analytical experiments were completed to break down the TCC cylinder bowl geometry by shifting the profundity of the bowls. The case with 1.26 mm decline top to bottom of the bowl from the benchmark TCC and covered with zirconium coating gives better results. TCC produced a very powerful squish over a short period of time. TCC's fraction of mass in carbon monoxide emissions is down to 0.03 at 25o crank angle after TDC while both hemispherical combustion chamber and shallow depth combustion chamber are measured at nearly 0.1. It was found that TCC gave a better performance compared with the other two designs at full load conditions while operating from medium to high engine speed. Overall, the low-speed application of the engine was suitable for SCC design, and TCC design was suitable for higher-speed application.

Keywords CI Engine · HCC · SCC · TCC · Aluminum · Zirconium · CFD

Abbreviations

TCC	Toroidal Combustion Chamber
HCC	Hemispherical Combustion Chamber
SCC	Shallow-depth Combustion Chamber
CFD	Computational Fluid Dynamics
BTE	Brake Thermal Efficiency
BSFC	Brake Specific fFuel Consumption
NOx	Oxides of Nitrogen
CO	Carbon Monoxide
HC	Hydrocarbon
PSZ	Partially Stabilized Zirconium
FTIR	Fourier Transform Infrared
FID	Flame Ionization Detector
GCMS	Gas Chromatography–mass Spectrometry
IW	Indicated Work
TDC	Top Dead Centre
HRR	Heat Release Rate

✉ C. Sakthi Rajan
   csrajann@gmail.com

1 SBM College of Engineering and Technology, Dindigul, Tamil Nadu, India 624 005

2 PSNA College of Engineering and Technology, Dindigul, Tamil Nadu, India 624 622

Introduction

Presently, extensive internal combustion (IC) engines are commonly used worldwide for transportation and stationary application. Attributable to stringent pollution requirements, many specialists searched for better engine frameworks with the least outflow. Oxides of nitrogen (NOx) and smoke outflows are the most acute problems in diesel-fueled compression-ignition (CI) engines [1–6]. Improving air–fuel blend, improved the execution of combustion engines. There were various approaches for improving the air–fuel blend inside a barrel, and one of approach is modifying the cylinder bowl geometry. Some scientists have chipped away at the chamber of ignition and the cylinder bowl geometry [7]. The burning of fuel/air was the development of manifold in base engines that exhibited a comfortable relationship with the geometry of cylinder bowls [8]. In their concern, different bowl geometries were examined with diesel and biodiesel in

the specific hemispherical combustion chamber (HCC), toroidal combustion chamber (TCC), and shallow-depth combustion chamber (SCC). The geometries of the three-cylinder bowls were considered and observed. The reduction of carbon monoxide (CO), hydrocarbon (HC), and smoke was decreased whereas NOx were greater in TCC as compared with HCC and SCC. TCC's were having the greater brake thermal efficiency (BTE). The geometry of the cylinder bowl was greater than the geometries of the SCC and HCC bowls. A replication report [9] showed that the cylinder bowl geometry influenced fuel burning and execution quality of conventional engines. Furthermore, these experiments were utilized to streamline the cylinder bowl geometry and the edge of the shower to enhance the execution and minimizing the discharge. The gas stream within the barrel was limited by swirling what's more, extreme dynamic vitality. Advanced cylinder bowl geometry alongside the swirl ratio was shown to decline fuel utilization and emanations [10]. The cylinder bowl geometry played a necessary part in fuel–air movement within the chamber. A high proportion of swirl generated by the cylinder bowl geometry provides proper mixing of air–fuel [11, 12]. The dimethyl ether utilized in the base engine and the advanced chamber to ignite the engine for different working conditions, were used. Five combustion geometries were investigated and found that deeper geometry of the metallic cylinder bowl is the best way to reduce the outflows of NOx, smoke, HC, and CO [13]. Furthermore, various kinds of geometries of cylinder bowls used were examined, for example, level and W-shaped bowls. However, a cylindrical bowl was shown to improve the mixing rate of air and fuel. A slight change in the cylinder bowl geometry greatly affects the whirl proportion and the choppiness force. The W-shaped bowl geometry delivered higher swirl and disturbance at TDC location when compared with level cylinder bowl. The three-dimensional (3D) computational fluid dynamics (CFD) when examined showed that the reenactments for stream of fuel–air blend

and swirl in case of re-contestant ignition cylinder [14]. Five distinctive cylinder bowl shapes were made and the outcomes approved with CFD investigations. Cylindrical-shaped bowls had influence on the stream fuel properties that is close to TDC. The investigation can possibly be planned to gear with higher execution and less outflows [15]. Break downs were seen even in diverse cylindrical-shaped bowls. Squish and swirl were found to assume an essential role in the cutting edge of a base engine. A coupling model utilizing the swirl, squish, disturbance, and cylinder bowl shape was made to achieve better ignition [16]. They performed analytical investigation on cylinder bowl geometry utilizing ANSYS. The four distinctive designs of a cylinder bowl, for example, level, slanted, focus bowl, and slanted counter balance bowl, were analyzed [17]. The results showed that focus bowl geometry performed much superior when compared with other bowl geometry shapes, since it delivered greater swirl direction. These criteria influence a remarkable role in conventional engine execution that decreases outflows. In the present examination, the impact of three fundamental features of cylinder bowls was examined for execution and discharge. The better execution of these fundamental features was further investigated by fluctuating deformation, strain, and stress of the piston when compared with aluminum. A solitary chamber direct infusion diesel engine was utilized for the present work. The standard cylinder of the engine was expelled and zirconium oxide (ZrO_2) was covered on the cylinder head as a warm hindrance covering by plasma splash process for the thickness of 100 μm. Zirconia, a clay material, has an extremely low warm conductivity values, great quality, and warm development coefficients like metals and can withstand higher temperature than metals.

Table 1 depicts the engine characteristics of fuels mixed with various nanoparticles. The upward direction symbolizes the increment, and the decrement is symbolized by the downwards direction.

Table 1 Characteristics of fuels mixed with various nanoparticles

Types of fuel	Nanoparticles	Performance		Emission				References
		BSFC	BTE	CO	NOx	HC	Smoke	
Biodiesel–JBO	Aluminium oxide (100 ppm)	↓	↑	↓	↓	↓	↓	[17]
	100 ppm of Ti_2O_3	↓	↑	↓	↓	↓	↓	
	CNT (100 ppm)	↓	↑	↓	↓	↓	↓	
Biodiesel–OLB	GO (100 ppm)	↓	↑	↓	↑	↓	↓	[18]
Biodiesel–GGB	CeO_2, ZrO_2, and TiO_2 (25 ppm)	↓	↑	↓	↑	↓	↓	[19]
Biodiesel–WCO	CeO_2 (80 ppm)	↓	↑	↓	↑	↓	↓	[20]
Biodiesel–PSB	SO (50 ppm)	↓	↑	↓	↑	↓	–	[21]
Biodiesel–BDB	CNT and AG (50 ppm)	↓	↑	↓	↑	↓	↓	[22]
Biodiesel–BDF	Nanosilver particles and CNT (40, 80, 120 ppm)	↓	↑	↓	↑	↓	↓	[23]

Characteristics of Borassus

Borassus flabellifer is a hefty tree of about 110 feet big. The leaves are 10–12 feet. The palm leaves are usually used in medical purpose. The palm tree is grown fantastically in Asian and Africans countries. Complete progression can be found in 5–7 yrs. The future changes from 85–105 yrs. The natural trees are insinuated as "Bandana" found in 3–5 numbers. Around 125–145 million of palmra palm lifer is grown about the globe. The oil was isolated from dried palm leaves life (Fig. 1).

Borassus oil extraction

Figure 1 depicts the extraction of palmyra palm leaves and Fig. 2 depicts the extraction of palmyra palm oil separately, as effective and moderate by various methods. The oil is extracted by solvent extraction that involves collecting 110 g of palmyra berry, drying and extracting using the aqueous extraction procedure with n-hexane in Soxhlet apparatus at 75 °C. The obtained oil extract is refined and subjected to evaporation in a rotating evaporator for 60 min, the oil was removed from the base Soxhlet apparatus. Finally, the biofuel oil is extracted from the seeds (Fig. 2) and the yield is determined.

Simulation and methodology

The current examination was performed ANSYS V18.1 software for CFD analysis on piston cylinder bowl geometries. Diverse info and limit conditions utilized for setting up the reproductions are recorded. These limits and introductory conditions continue as before for all the cases [18]. To look the outcomes, limit conditions were kept consistent for each case. All the basic states of the diversion were
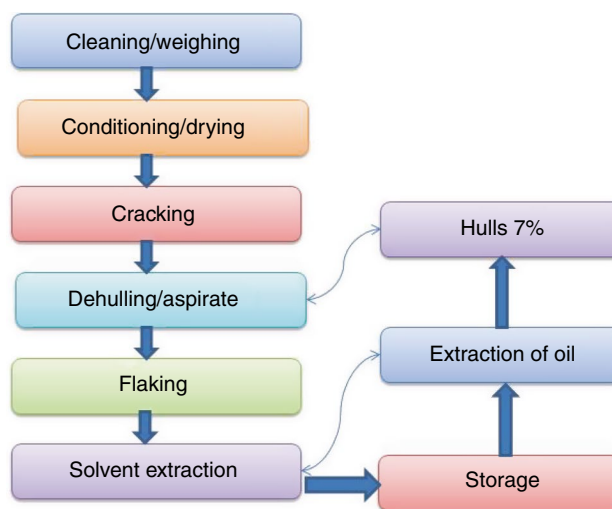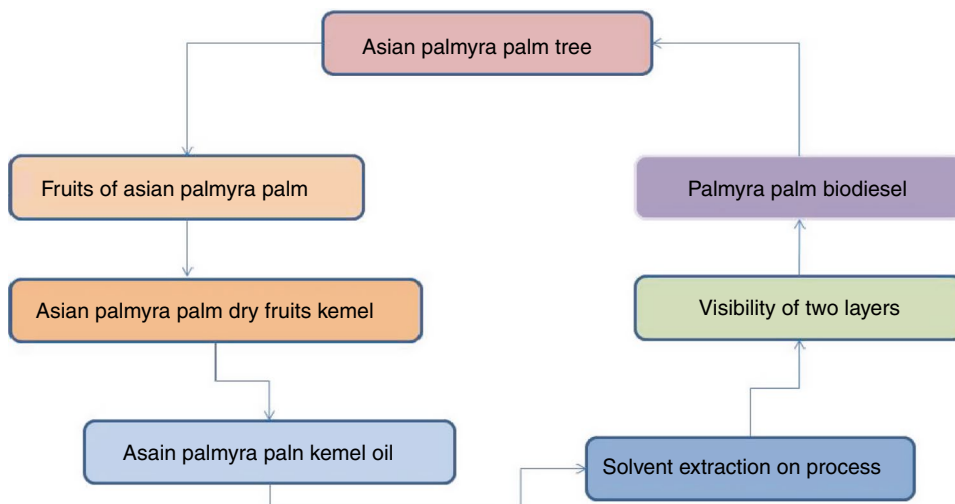

Fig. 2 Extraction of oil

taken at the IVC. ANSYS ascertains the response rates for each rudimentary attitude; meantime, the CFD explains the vehicle conditions. SAGE can be utilized for demonstrating numerous ignition systems (pressure, choppiness dynamic, temperature, and speed).

Experimental diesel engine setup

Figure 3 shows the engine setup. The current investigation was conducted on a single cylinder DI base engine manufactured by Kirloskar. This base engine produces 3.5 kW and operates at a speed of 1500 rpm. With stroke and bore, this base engine with connecting rod had a fuel capacity of 7 L. (112 and 88.7 mm). This engine was run at 17:1 compression ratio, as recommended by the engine manufacturer. The MICO-based engine management system and piezoelectric

Fig. 1 Extraction of oil from palmyra palm

Fig. 3 Engine setup
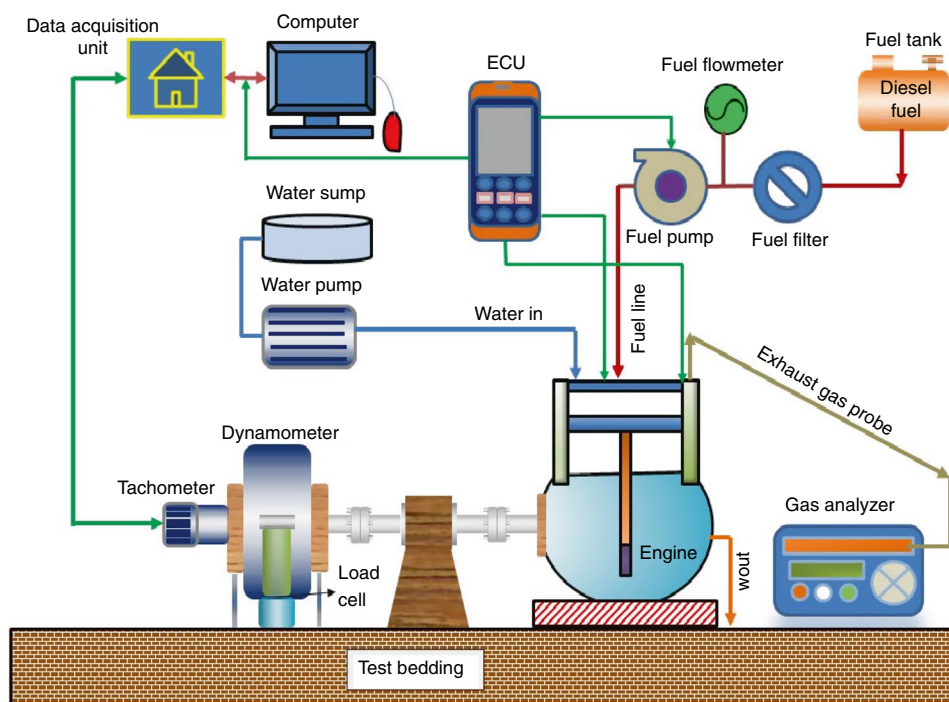
pressure gauge were used in this experiment to evaluate the combustion process of the base engine [19–21].

The QRO-402 tailpipe analysis tool was used to test the tailpipe characteristics such as HC, NOx, and CO, and the AVL437C smoke metre was used to test the opacity of smoke. The base engine was connected to a dynamometer to generate various loading conditions, and thus the base engine has been run from low to high operating conditions [22, 23]. The experiment was carried out from 0 to 100% operating conditions. This base engine was cooled by natural air, and SAE40 lubricant (3.8 L) was used at 85 °C to prevent corrosion between engine parts. Table 1 reveals the engine specifications for this diesel engine. Meanwhile, to surveillance the heat release of engine oil, tailpipe emissions and delivered heat to the atmosphere was calculated by the temperature sensors fitted to the engine. The engine specification is shown in Table 2. Tables 3 and 4 depict the fuel properties and the properties of different ceramics materials.

Coating materials

The cylinder piston was coated with zirconium and aluminum using the plasma spray method. This method gave better stability when compared with other coating materials. The preferred coating thickness used is 0.5 mm or 500 μ, especially the thickness below 0.5 mm is not stable. The piston top face, inlet value, and outlet value are coated with the coating of 0.5 mm thickness. The coated piston is shown in Fig. 4.

Table 2 Engine specifications

Diameter of bore	87.5 mm
Length of stroke	110 mm
Length of the rod	245 mm
Pressure	200 bar
Speed	1500 rpm
Rated power	5.1 kW
MFI (kg/cycle)	2.67765–05e
Exhaust value	6° BTDC @ 0.15 mm lift
Inlet value	2° BTDC @ 0.15 mm lift
CR	17.5
SI	–23 degree
Injection duration (CAD)	22 degree
Timing of inlet vale	IVO–184.5_ATDC
Timing of outlet vale	EVO 144.5_ATDC
Temperature of piston (K)	523

Table 3 Fuel properties

Properties	D100	BF100	BF20
Density/g m^{-3}	0.86	0.89	0.83
Viscosity/mm^2 s^{-1}	2.95	4.3	3.19
Calorific value/MJ kg^{-1}	44	41	43.76
Flashpoint/°C	47	152	52
Create index	53	51	56
Cloud point/°C	0	2	5
Pour point/°C	–11	–6	–8

Effects of partially stabilized zirconia fueled with Borassus biofuel at different piston...

8905

Table 4 Properties of different ceramics materials

Property	Zirconium	Aluminum	Silicon
Density/g cm^{-3} at 20 °C	6.49	5.54	4.23
Melting point/°C	1852	2,072	1358
Boiling point/°C	4400	2,977	2724
Atomic number	40	56	74
Atomic mass/g mol^{-1}	91.22	101.90	95.34

FTIR analysis

The specimen was stacked in the FTIR spectroscopy, coated with the biodiesel, and the results of the FTIR analysis is shown in Fig. 5. The FTIR showed that the biodiesel had peak –CH band at 1700–3000 cm^{-1} and N–H band at 1236 cm^{-1} confirming the presence of biomolecules in the biodiesel. Similarly, at peak 2954 cm^{-1} the presence of N–H band was seen and it was more extensive than other peaks. Apart from this, the in-plane amine (NH$_2$) band was seen at 1457 cm^{-1} (wide band ring at 805.1 cm^{-1}) and the peaks of –CH$_3$ and C–H bands were at 1457 and 2954 cm^{-1}, respectively. Further, the peak of C=O band was seen at 1457 cm^{-1}.

Gas chromatography (GC)

The non-polar model of the capillary type SLB-5 MS was used as a column along with 10 m×0.10 mm ID and 0.10 μm films which are prepared for analysis. For this analysis, the oven was heated at a rate of 85.7 cm s^{-1} (constant) at 42 °C and 55 °C min^{-1} at 330 °C with the carrier gas of influential hydrogen. The injection speed of 0.5 μL with the ratio of 300:1 at the desired temperature of 330ºC and flame ionization detection (FID) detector was used to inspect the sample. The GC analysis results of biodiesel are displayed in Fig. 6.

HCC, SCC, and TCC

For HCC design, the velocity contours in the piston were obtained using ANSYS V18.1, as shown in Fig. 7. For SCC design, the velocity contours in the piston were obtained using ANSYS V18.1, as shown in Fig. 8. For TCC design, the velocity contours in the piston were obtained using ANSYS V18.1, as shown in Fig. 9.

Results and discussions

The simulation of various designs of the piston was performed on ANSYS V18.1. This section discusses the deformation, stress, and strain of the aluminum piston and compared with the zirconium-coated piston.

Fig. 4 Coated piston
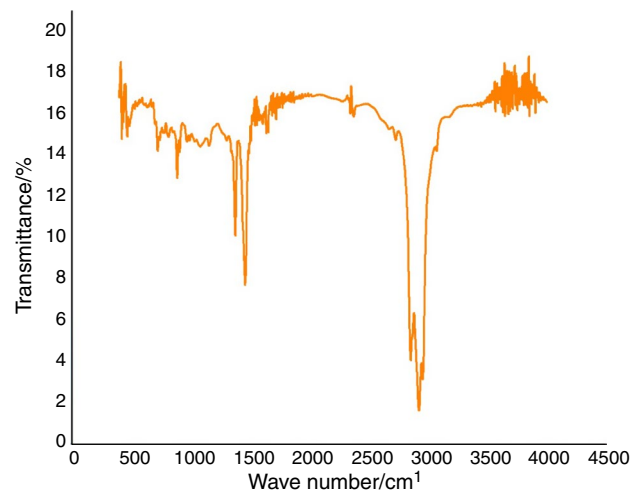
Fig. 5 FTIR analysis

Deformation analysis

For the deformation test, the temperature on the piston between aluminum and zirconium-coated piston was almost 534°K. Deformation occurs under the static structure of complete deformation was represented in mm. After heat gets desired from the outer source piston and tries to conform to some other structure from this original structure. The maximum deformation level in the aluminum-coated piston was nearly 0.189 mm and when the heat was applied to the coated zirconium the deformation level was evidently seen at 0.1411 mm, as shown in Figs. 10 and 11, respectively.

Stress analysis

In the stress test, the pressure on the piston between the aluminum and zirconium-coated piston was kept around 280 bar. For stress analysis, ANSYS Static Structure tool was utilized for total stress in MPa. After applying load
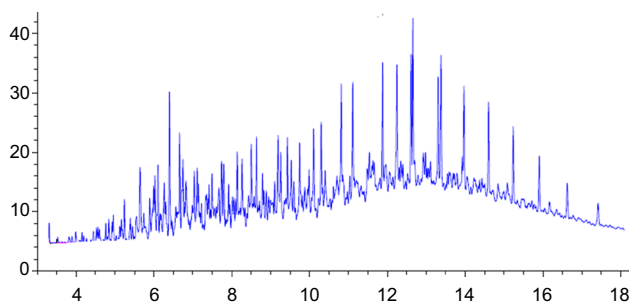
Fig. 6 GC–MS analysis

from the outer surface of piston head, the stress from the original structure to the other structure was also calculated. For aluminum piston the maximum stress level was nearly 466.66 mm, and when the load was applied to the coated zirconium piston, the deformation level was approximately 488.41 mm, as shown in Figs. 12 and 13, respectively.

Strain analysis

Analysis of strain for the aluminum and zirconium-coated piston under the pressure inside the piston of 280 bar was performed. For strain analysis (in mm), ANSYS Static Structure tool was utilized. Load was applied on the outer surface of piston head and the strain from the original structure to the deformed structure was calculated [24]. The maximum strain level of the aluminum was about 0.0065849 mm and when the load was applied on the coated zirconium the deformation level was about 0.0048877 mm, as shown in Figs. 14 and 15, respectively.

Thermal stress analysis

Figures 16 and 17 showed the piston with coating and without coating under total heat fluxes, respectively. The effect of stress investigation and thermal analysis were attributed to the merged field assessment and the reliant on one another. The static thermal examination was first performed under thermal limits, and the consequences under the thermal stress were then assessed. In an ideal condition, the temperature of chamber was given as the additional data along with pressure load. At last, the combined thermal investigation, thermal strain, and scattering of temperature by the piston with coating and without coating were analyzed.

The images clearly show the top face of the piston exhibiting maximum stress acting (shown in red color) and the minimum stress acting on the top face of the piston (shown in green colour) both in the coated and uncoated piston.

Finite element analysis for piston

Figures 18 and 19 depict the temperature distributions on the uncoated and coated piston. CATIA part design enables multiple stages of product development from conceptualization, design and engineering to manufacturing. The red shades shown depicts the most extreme pressure zone especially on top of the cylinder, and the blue shades depicts the least pressure zone especially on the base pressure of the cylinder's base, both in the coated and uncoated cylinders.

The diminished in heat progress and supported the thermal distribution in a segment of the conventional engine with coated piston were evaluated. A chamber was chosen, considering it as the engine essential portions for FEA heat transmission. The preliminary division, the elements types of quadratic 189 SOILD-20 node aspects of greater-request of greater-demand for cross section the solid chamber count, concurring interest, and association test. For a reasonable limit executed to settle the best number of parts, the most essential temperature was considered. Table 4 shows the eventual outcomes. Higher-demand parts were esteemed with 100% exactness for making the chamber math, as laid out in Fig. 19.

Performance

Indicated work

Figure 20 shows that variation of engine speed with indicated work (iw). Variations of established iw delivered for three types of design bowl geometries at the base engine for different engine speeds of 1200, 2400, and 3600 rpm under partially load conditions. The engine speed was increased to give the better performance and it clearly showed that the speed of 2400 and 3600 rpm to give better performance for tcc piston design then compared with the hcc and scc pistons design. Since, the tcc design produced the powerful squish as it can be observed from the figure that the direction of velocity vector and magnitude were higher for tcc design [25]. henceforth, making an all the more homogeneously spread fuel–air blend, what's more, improving fuel dissipation process, in this manner a superior and progressively exceptional ignition directly after the tdc. As a conclusion, from 2400 rpm to maximum speeds, tcc design showed the best performance [26].

In any case, an inconsistency happened in the combustion chamber at 1200 rpm speed due to which scc obtained greater iw correlated to tcc. Two potential reasons are seen in scc at minimum speed of engine [27]. The principal
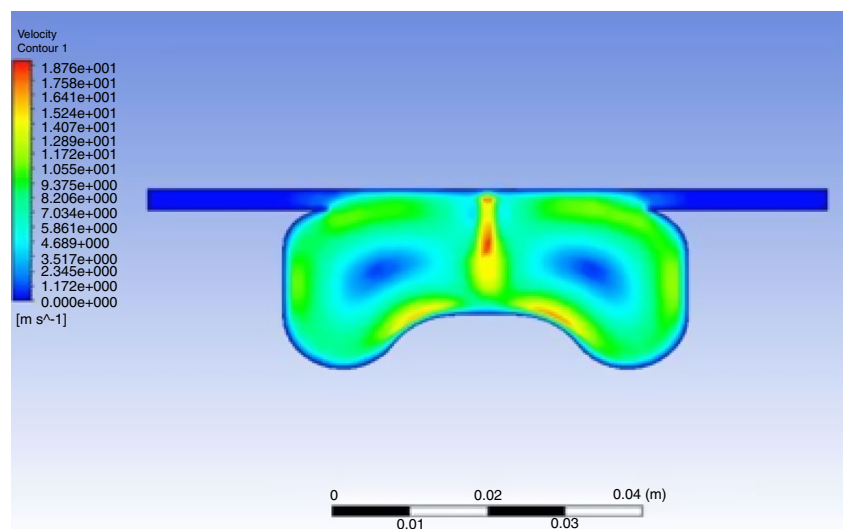
Fig. 7 Hemispherical combustion chamber designs that are represent a velocity motion in the piston
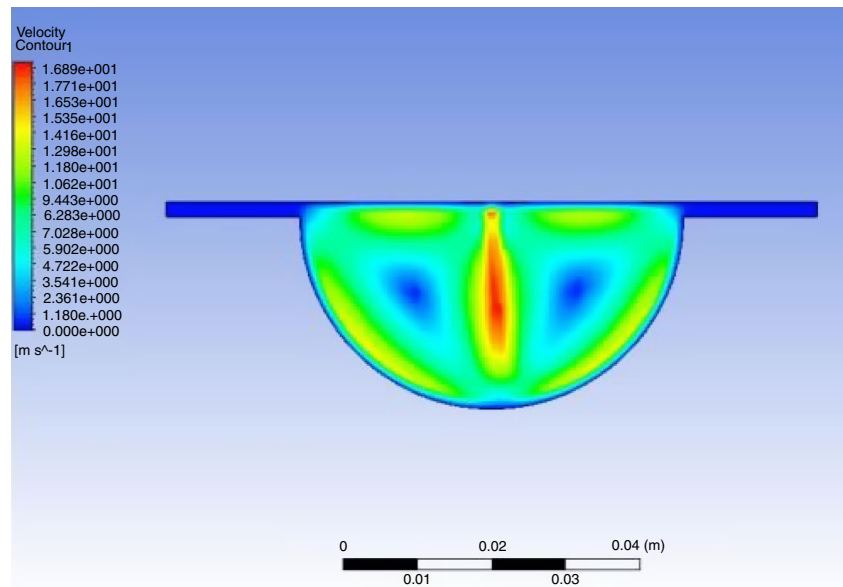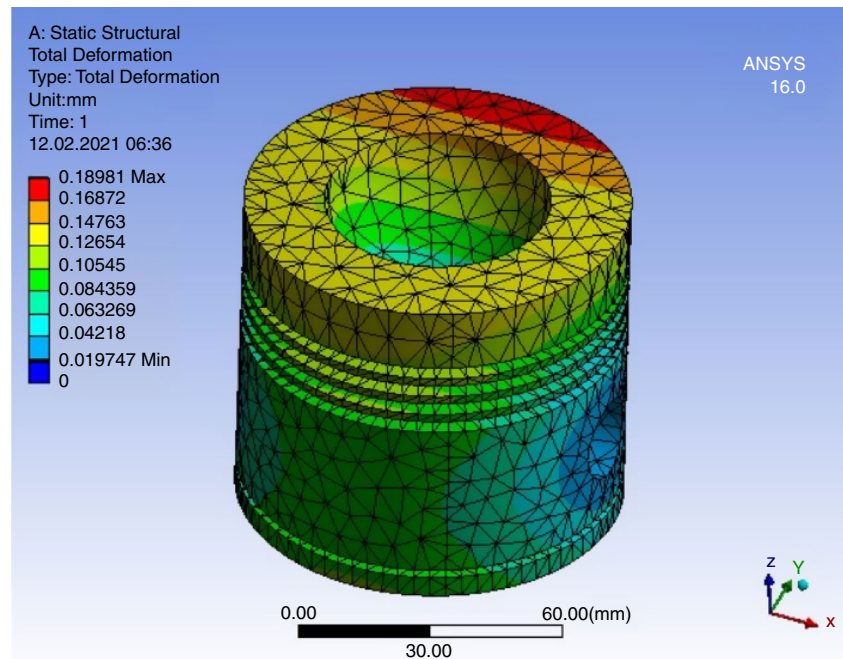

Fig. 8 Toroidal combustion chamber design that are represent a velocity motion in the piston
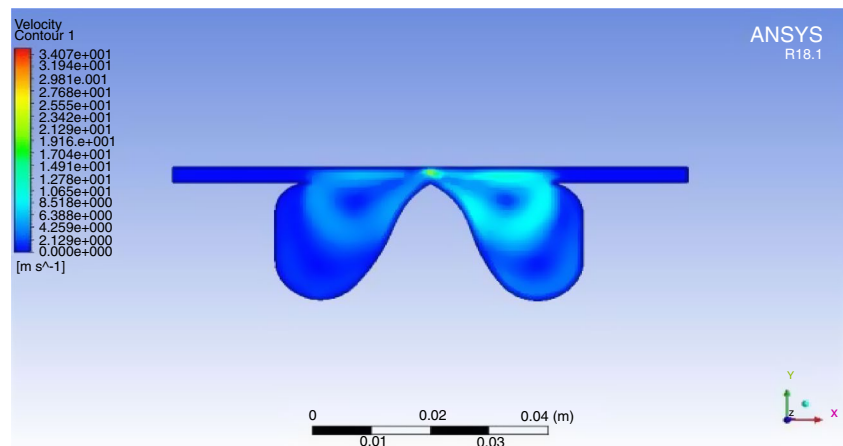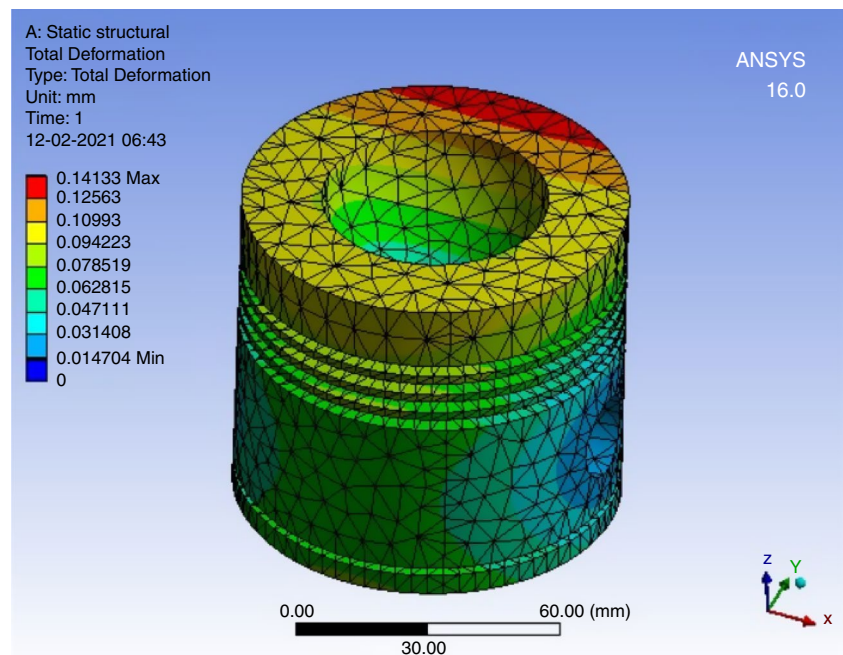

Fig. 9 Shallow depth combustion chamber designs that are represent a velocity motion in the piston

Fig. 10 Deformation of coated aluminum piston

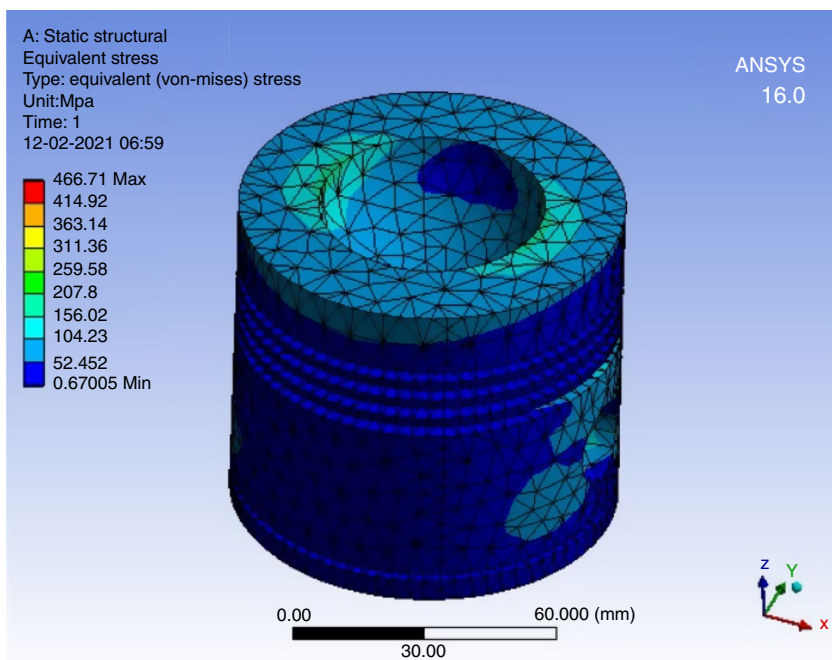**Fig. 11** Deformation of coated zirconium piston

reason goes to the way that lower speed of engine provides an adequate time to fuel–air blending which reduced the impact of bowl design geometry motion of air in real-time movement on the ignition process [28]. Another reason is due to the loss of heat through the ignition process. As described above, the geometry layout of the tcc bowl has an evidently bigger volume to surface area ratio, which is contrasted to the geometry of the shallow depth combustion bowl thus heat losses are more at low engine speeds during a longer ignition process [29].

It can be observed clearly that hcc design has lesser indicated work when compared with scc at a minimum speed

Fig. 12 Stress analysis coated aluminum piston

**Fig. 13** Stress analysis of coated zirconium piston
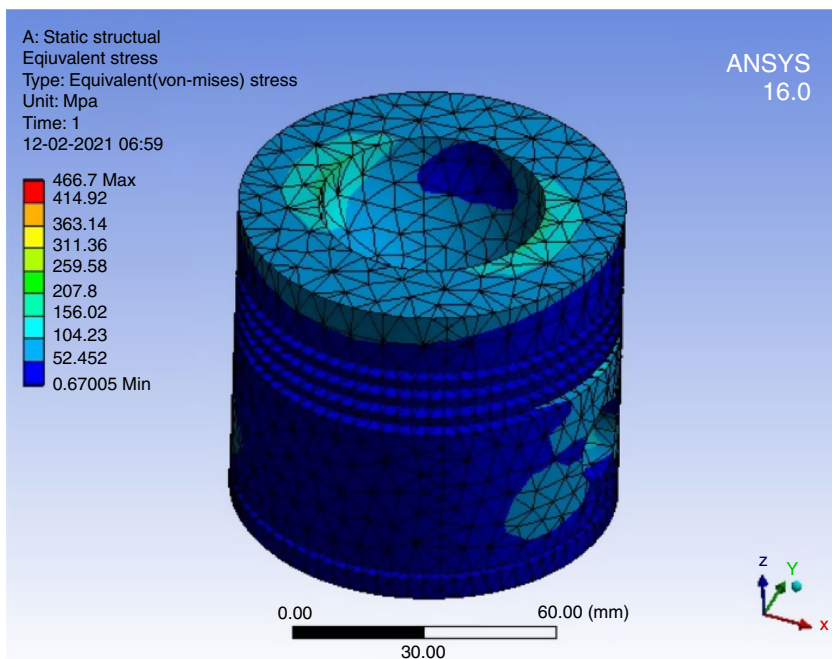
of up to 1200 rpm, since the hcc design created more turbulence when compared with to scc, causing some portion of the tested fuel stores in that internal surface and breaking down the dissipation of tested fuel, that regulates the ignition process; therefore, the hcc design engine receives a lower exhibited energy [30]. When operating an engine at the speeds of 2400 and 3600 rpm, the impact of enlarged hemispherical combustion chamber disturbance exceeded the adverse impact of decreased penetration size, thereby obtaining a greater ip for the hcc engine design.

Fig. 14 Stress analysis of coated aluminum piston
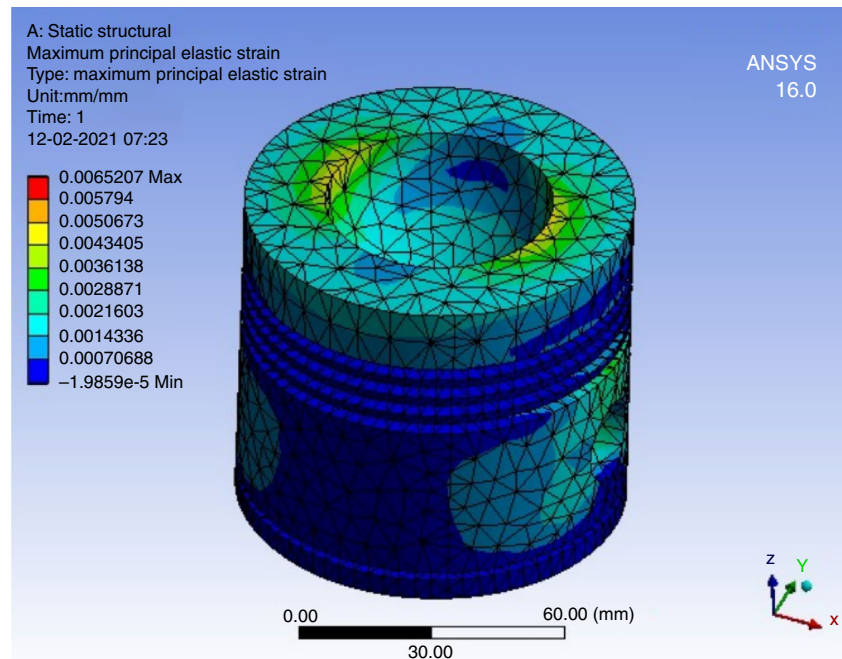
**Fig. 15** Stress analysis of coated zirconium piston
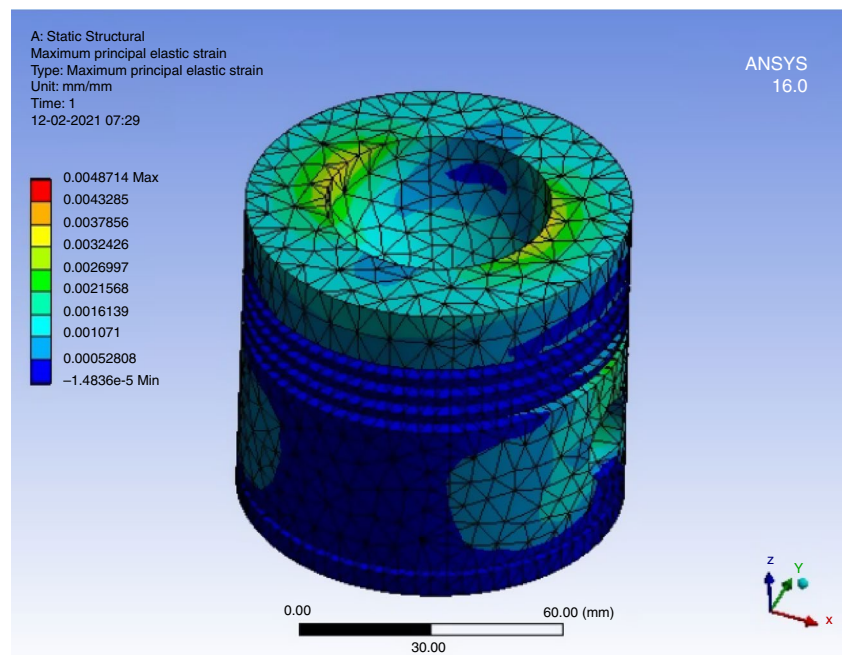

Cylinder pressure

In order to obtain a superior perceptive of the combustion process, the cylinder pressure (CP) versus the CA for specific geometric design bowl conditions, such as HCC, SCC, and TCC, compared with different rotation speeds of 1200, 2400 and 3600 rpm at full load as shown in Figs. 21–23. It is shown that SCC marginally has greater pressure after 15° crank angle is correlated with hemispherical combustion chamber and TCC at engine speed is 1200 rpm which further explains SCC's most significant exhibited operation among the three bowl geometries [31]. The SCC and HCC

Fig. 16 Heat flux distribution with coated piston
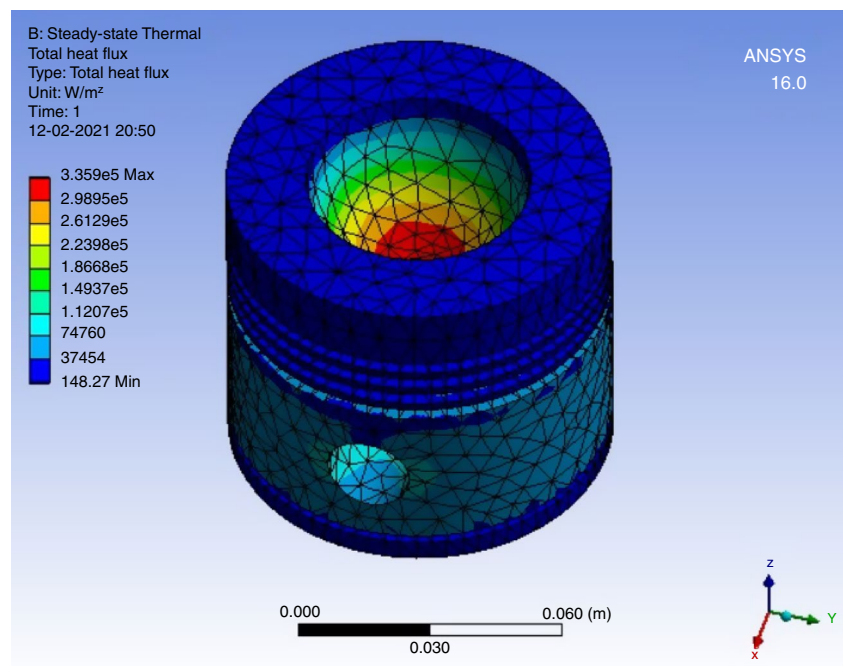
**Fig. 17** Heat flux distribution without coated piston
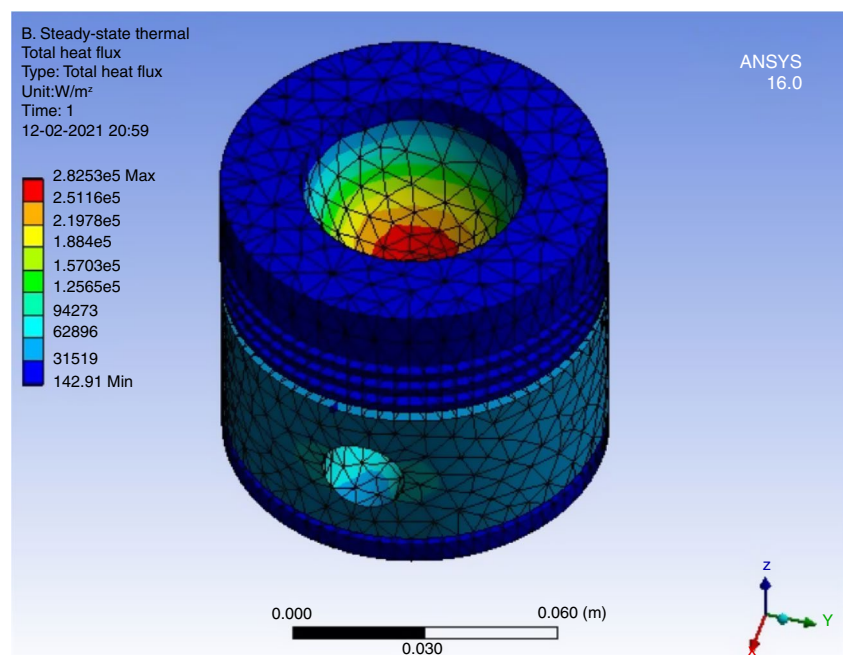
enhanced the maximum pressure because of the heat losses and motion of squish while increasing the engine speed. As a result, SCC will have a greater pressure peak at minimum speed of the engine whereas TCC will have a greater pressure peak from average to high engine speed [32].
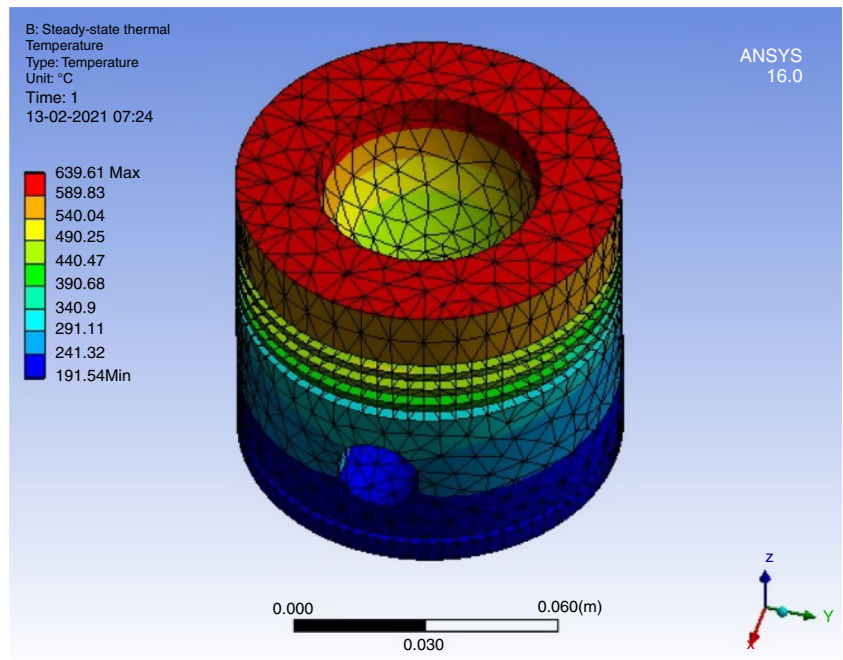
Heat release rate

The heat release rate (HRR) versus CA for various geometric bowl conditions like HCC, SCC, and TCC compared for different speeds of 1200, 2400, and 3600 rpm at full load condition as shown in Figs. 24–26, respectively. The HRR

Fig. 18 Temperature distribution without coated piston
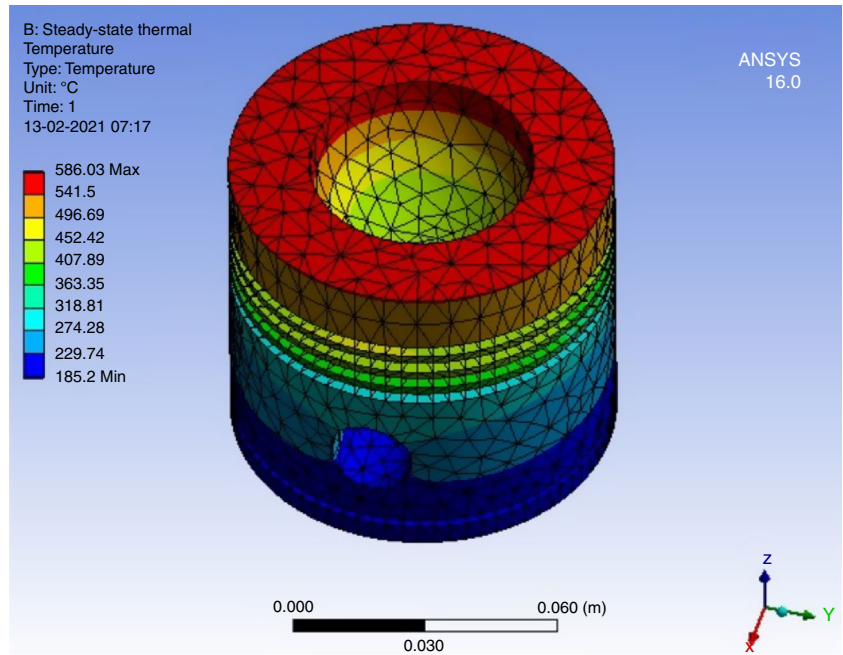
Fig. 19 Temperature distribution with coated piston

still increased when the in-cylinder pressure was elevated. It is shown that the maximum peak rate reached at speed of 1200 rpm during the combustion phase occurred at 12° crank angle with shallow depth combustion chamber which is related to the most noteworthy demonstrated peak pressure and work at similar conditions [33]. There are two major factors that are already described in the introduction section. The SCC design enhanced the engine speed during medium load conditions, but lowered the heat release rate at different speeds of 1200, 1600, and 3600 rpm. However, it should be mentioned that at higher engine speed the absolute time-limit is lowered [34]. Meanwhile, under high engine speed conditions TCC poses a faster in heat discharge as shown in Fig. 20, showing TCC's more powerful performance at a speed of 3600 rpm.

Carbon monoxide

The variation of CO emission versus crank angle for various geometric bowl conditions like HCC, SCC, and TCC compared at different speeds of 1200 and 3600 rpm at full load condition as shown in Fig. 27. It is shown that the CO emission was produced when the engine speed after the top dead center (TDC) is progressively increased [35]. Finally reaching peak, CO is rapidly oxidized, particularly for shallow depth combustion chamber which appearances the lesser CO fraction of mass at 25° crank angle after TDC. Additionally, this is an indication of the moderate shorter ignition timing

in shallow depth combustion chamber design geometry in contrast to the other two types of design parameters at lesser speed of engine. At 3600 rpm of speed of the engine, however, in TCC bowl geometry, the oxidation of CO emissions is faster contrasted with other bowl shapes. TCC's fraction of mass in carbon monoxide emissions is down to 0.03 at 25° crank angle after TDC while both hemispherical combustion chamber and shallow depth combustion chamber are measured at nearly 0.1 [36]. As discussed, proper mixing does not takes place for shallow depth combustion chamber due to the low consequences of the vector velocity at greater speed of the, due to greater carbon monoxide tailpipe emissions. Conversely, the squish motion of TCC at greater speed of the engine is progressively important, however, regulates the refusal impact of expanded heat losses, thus reducing the CO tailpipe emission compared to the other two bowl geometries.

Oxides of nitrogen

The NOx emission versus crank angle for various geometric design like HCC, SCC, and TCC at different speeds of 1200, 2400, and 3600 rpm while maintaining full load condition is shown in Fig. 28. At 1200 rpm, the highest NOx was observed for SCC when compared with HCC and TCC. The high temperature produced during the process of combustion is the major reason for the increase in oxides of nitrogen [37]. It is observed that the mass fraction was high in
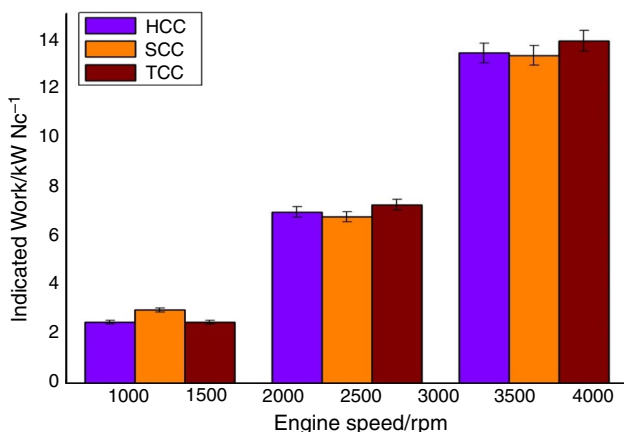

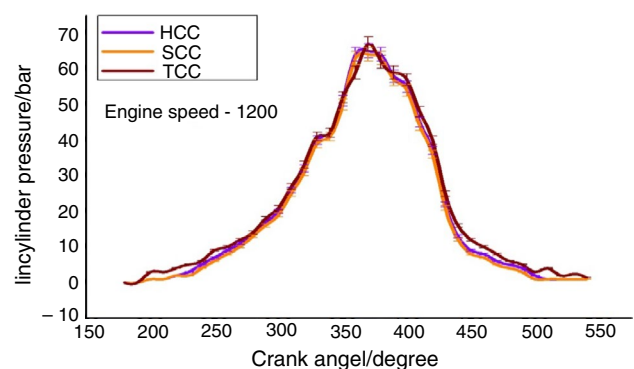**Fig. 20** Variations of engine speed versus indicated work
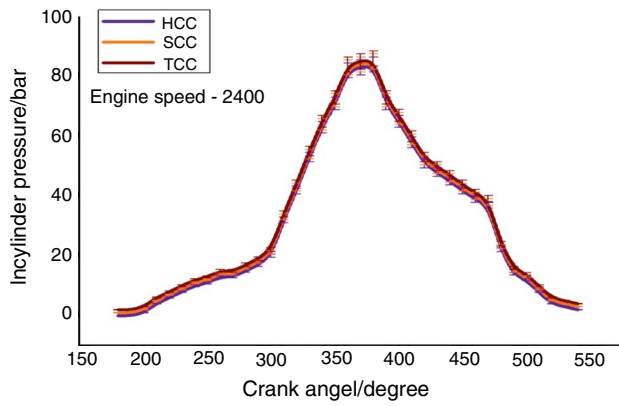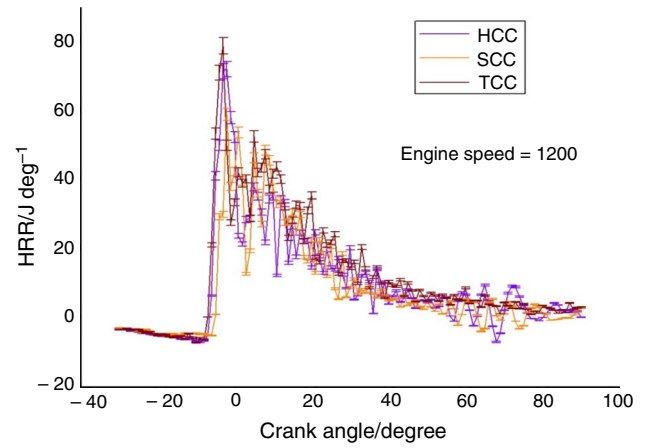

Fig. 21 Variations of crank angle versus in-cylinder pressure at 1200 rpm
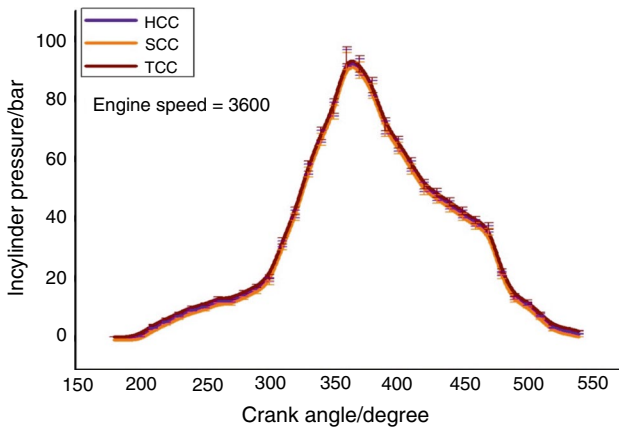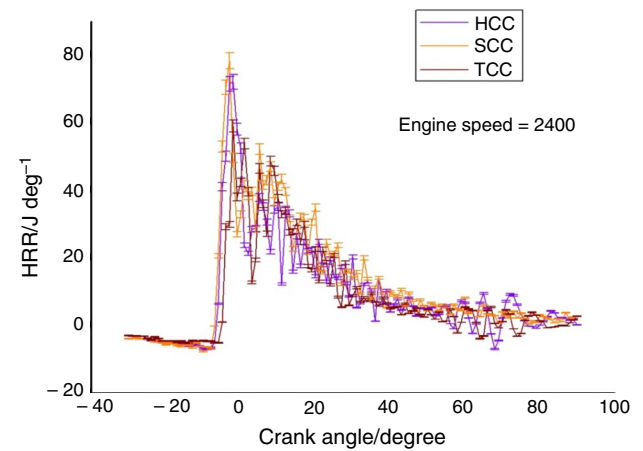
Fig. 22 Variations of crank angle versus in-cylinder pressure at 2400 rpm

Fig. 24 Variations of crank angle versus HRR at 1200 rpm

Fig. 23 Variations of crank angle versus in cylinder pressure at 3600 rpm

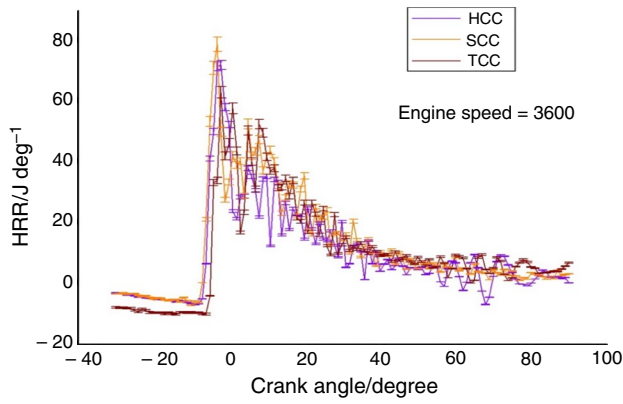**Fig. 25** Variations of crank angle versus HRR at 2400 rpm

Fig. 26 Variations of crank angle versus HRR at 3600 rpm

TCC design thus NOx emission at speed of 3600 rpm, however, lower emissions were achieved with SCC design bowl geometry [38]. The SCC has the lowest HRR that provided a longer duration. Because of the discharge of total heat for equivalent in all bowl design geometries at the diesel engine's equal rpm, the greater discharge of heat process along with low heat discharge is an opportunity for longer period of lesser temperature produced in combustion at each crank angle [39]. In this context, the most minimal NOx emission is for SCC bowl geometry [12]. Again, the NO$_x$ emission produced for TCC bowl design geometry is the most significant which led to the massive disturbance and the greater heat release rate value which is shown in Fig. 22.
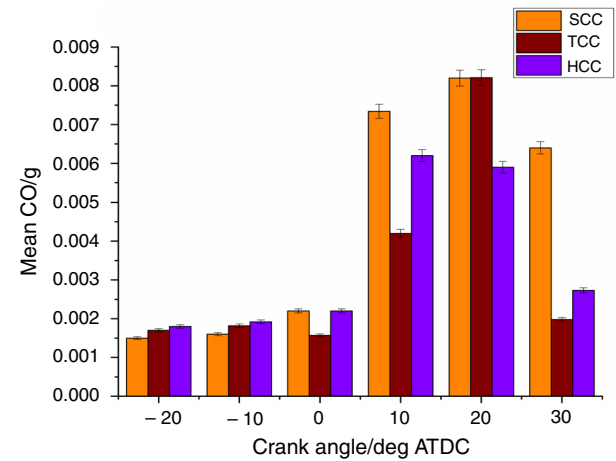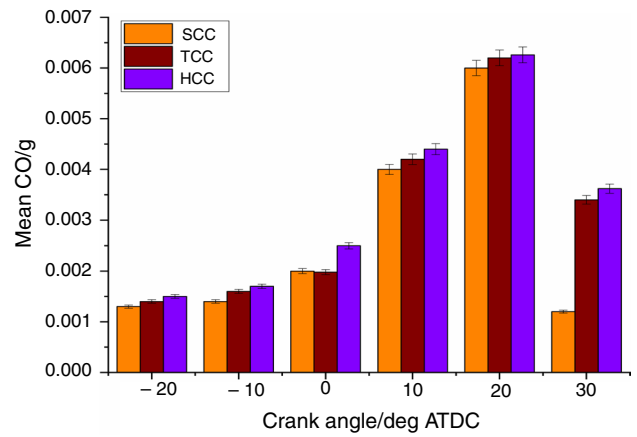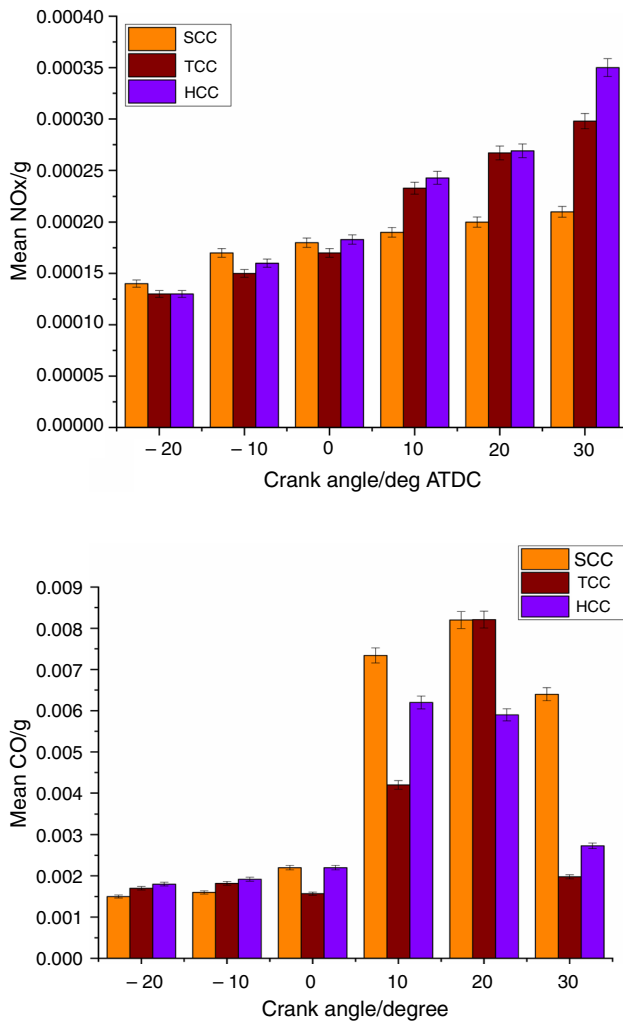

Fig. 27 Variations of crank angle versus mean CO at 2400, and 3600 rpm

Fig. 28 Variations of crank angle versus mean NOx at 2400, and 3600 rpm

- The SCC showed a superior performance, heat release rate, and higher cylinder pressure and indicator work when correlated with TCC and HCC at lower engine speed. At lower engine speed the SCC design is described as the optimum when compared with the other two designs.
- Across the whole combustion process, TCC produced a very powerful squish over a short period of time. It is illustrated the TCC showed better performance when compared with the other two designs at full load conditions from medium to high engine speed.
- The conclusion for the research work is that low-speed operation of the engine condition is suitable for SCC design, and that TCC design is suitable for high-speed operation of the engine.

References

1. Kumar S, Kumar Chauhan M, Varun. Numerical modeling of compression ignition engine: a review. Renew Sustain Energy Rev [Internet]. Elsevier; 2013;19:517–30. Available from: https://doi.org/10.1016/j.rser.2012.11.043.
2. Diaz P. Computational optimization of internal combustion engines. Comput Optim Intern Combust Engines. 2014.
3. Elumalai PV, Annamalai K, Dhinesh B. Effects of thermal barrier coating on the performance, combustion and emission of DI diesel engine powered by biofuel oil–water emulsion. J Therm Anal Calorim [Internet]. Springer International Publishing; 2019;137:593–605. Available from: https://doi.org/10.1007/s10973-018-7948-6.
4. Perumal Venkatesan E, Kandhasamy A, Sivalingam A, Kumar AS, Ramalingam KM, Joshua P james thadhani, et al. Performance and emission reduction characteristics of cerium oxide nanoparticle-water emulsion biofuel in diesel engine with modified coated piston. Environ Sci Pollut Res. 2019;26:27362–71.
5. Perumal Venkatesan E, Kandhasamy A, Subramani L, Sivalingam A, Senthil KA. Experimental investigation on lemongrass oil water emulsion in low heat rejection direct ignition diesel engine. J Test Eval. 2019;47:20170357.
6. Parthasarathy M, Ramkumar S, Isaac JoshuaRamesh Lalvani J, Elumalai PV, Dhinesh B, Krishnamoorthy R, et al. Performance analysis of HCCI engine powered by tamanu methyl ester with various inlet air temperature and exhaust gas recirculation ratios. Fuel [Internet]. Elsevier; 2020;282:118833. Available from: https://doi.org/10.1016/j.fuel.2020.118833.
7. Abdul Gafoor CP, Gupta R. Numerical investigation of piston bowl geometry and swirl ratio on emission from diesel engines. Energy Convers Manag [Internet]. Elsevier Ltd; 2015;101:541–51. Available from: https://doi.org/10.1016/j.enconman.2015.06.007.
8. Jaichandar S, Annamalai K. Influences of re-entrant combustion chamber geometry on the performance of Pongamia biodiesel in a DI diesel engine. Energy [Internet]. Elsevier Ltd; 2012;44:633–40. Available from: https://doi.org/10.1016/j.energy.2012.05.029.
9. Lim J, Min K. The effects of spray angle and piston bowl shape on diesel engine soot emissions using 3-D CFD simulation. SAE Tech Pap. 2005.

Conclusions

- In this study, the numerical investigation was conducted to see the impact of various cylinder bowl geometries at consistent speed and load using ANSYS V 18.1. Recent results showed that the shape of the TCC cylinder bowl in reference to ISFC was observed to be the best of the three geometries. The tests were extended to evaluate the TCC bowl shape's pressure, strain, and stress attributes. Lessening bowl all-around from TCC design (21.56–20.30 mm) enhances ignition and further reduction from top to bottom of bowl contributes to breakdown in performance. The life expectancy of cylinder can be increased by using zirconium coating. In the analysis part it is clearly understand with coating of piston the temperature act more in the piston when compared with the uncoated piston.

10. Ramesh Bapu BR, Saravanakumar L, Durga Prasad B. Effects of combustion chamber geometry on combustion characteristics of a DI diesel engine fueled with calophyllum inophyllum methyl ester. J Energy Inst. [Internet]. Elsevier Ltd; 2017;90:82–100. Available from: https://doi.org/10.1016/j.joei.2015.10.004.

11. Fuchs TR, Rutland CJ. Intake flow effects on combustion and emissions in a diesel engine. SAE Tech Pap. 1998.

12. Park S. Optimization of combustion chamber geometry and engine operating conditions for compression ignition engines fueled with dimethyl ether. Fuel [Internet]. Elsevier Ltd; 2012;97:61–71. Available from: https://doi.org/10.1016/j.fuel.2012.03.004.

13. Béard P, Mokaddem K, Baritaud T. Measurement and modeling of the flow-field in a di diesel engine: Effects of piston bowl shape and engine speed. SAE Tech Pap. 1998.

14. Prasad BVVSU, Sharma CS, Anand TNC, Ravikrishna RV. High swirl-inducing piston bowls in small diesel engines for emission reduction. Appl Energy [Internet]. Elsevier Ltd; 2011;88:2355–67. Available from: https://doi.org/10.1016/j.apenergy.2010.12.068.

15. Payri F, Benajes J, Margot X, Gil A. CFD modeling of the in-cylinder flow in direct-injection Diesel engines. Comput Fluids. 2004;33:995–1021.

16. Song J, Yao C, Liu Y, Jiang Z. Investigation on flow field in simplified piston bowls for Di diesel engine. Eng Appl Comput Fluid Mech. 2008;2:354–65.

17. Gnana Sagaya Raj AR, Mallikarjuna JM, Ganesan V. Energy efficient piston configuration for effective air motion—a CFD study. Appl Energy [Internet]. Elsevier Ltd; 2013;102:347–54. Available from: https://doi.org/10.1016/j.apenergy.2012.07.022.

18. Senecal PK, Pomraning E, Richards KJ, Briggs TE, Choi CY, McDavid RM, et al. Multi-dimensional modeling of direct-injection diesel spray liquid length and flame lift-off length using cfd and parallel detailed chemistry. SAE Tech Pap. 2003.

19. Sivalingam A, Kandhasamy A, Senthil Kumar A, Perumal Venkatesan E, Subramani L, Ramalingam K, et al. Citrullus colocynthis—an experimental investigation with enzymatic lipase based methyl esterified biodiesel. Heat Mass Transf und Stoffuebertragung. Heat and Mass Transf. 2019;55:3613–31.

20. Elumalai PV., Nambiraj M, Parthasarathy M, Balasubramanian D, Hariharan V, Jayakar J. Experimental investigation to reduce environmental pollutants using biofuel nano-water emulsion in thermal barrier coated engine. Fuel. 2021;285.

21. Elumalai PV, Balasubramanian D, Parthasarathy M, Pradeepkumar AR, Mohamed Iqbal S, Jayakar J, et al. An experimental study on harmful pollution reduction technique in low heat rejection engine fuelled with blends of pre-heated linseed oil and nano additive. J Clean Prod [Internet]. Elsevier Ltd; 2021;283:124617. Available from: https://doi.org/10.1016/j.jclepro.2020.124617.

22. Jayakar J, Elumalai A, Mailainathan M, Dhinesh B, Harikrishnan G. Macroscopic characteristics of palm oil and palm oil methyl ester using dimensionless analysis. J Oil Palm Res. 2018;30:666–73.

23. Elumalai PV, Sivakandhan C, Parathasarathy M, Mohamad Iqubal S, Arunkumar M. Investigation on the mitigation of environmental harmful emissions by incorporating nanoparticles to biofuel water nano emulsion in low heat rejection engine. Heat Mass Transf und Stoffuebertragung. Heat and Mass Transf. 2021.

24. Schmidt DP, Rutland CJ. A new droplet collision algorithm. J Comput Phys. 2000;164:62–80.

25. Liu AB, Mather D, Reitz RD. Modeling the effects of drop drag and breakup on fuel sprays. SAE Tech Pap. 1993.

26. Post SL, Abraham J. Modeling the outcome of drop-drop collisions in Diesel sprays. Int J Multiph Flow. 2002;28:997–1019.

27. Gonzalez DMA, Lian ZW, Reitz RD. Modeling diesel engine spray vaporization and combustion. SAE Tech Pap. 1992.

28. Isaac Premkumar IJ, Prabhu A, Vijayan V, Godwin Antony A, Venkatesh R. Combustion analysis of biodiesel blends with different piston geometries. J Therm Anal Calorim [Internet]. Springer International Publishing; 2019; Available from: https://doi.org/10.1007/s10973-019-09144-1.

29. Chiang CH, Raju MS, Sirignano WA. Numerical analysis of convecting, vaporizing fuel droplet with variable properties. Int J Heat Mass Transf. 1992;35:1307–24.

30. Rajendran S. A comparative study of performance and emission characteristics of neat biodiesel operated diesel engine: a review. J Therm Anal Calorim [Internet]. Springer International Publishing; 2020; Available from: https://doi.org/10.1007/s10973-020-10121-2.

31. Subramaniam M, Solomon JM, Nadanakumar V, Anaimuthu S, Sathyamurthy R. Experimental investigation on performance, combustion and emission characteristics of DI diesel engine using algae as a biodiesel. Energy Reports [Internet]. Elsevier Ltd; 2020;6:1382–92. Available from: https://doi.org/10.1016/j.egyr.2020.05.022.

32. Muše A, Jurić Z, Račić N, Radica G. Modelling, performance improvement and emission reduction of large two-stroke diesel engine using multi-zone combustion model. J Therm Anal Calorim [Internet]. Springer International Publishing; 2020;141:337–50. Available from: https://doi.org/10.1007/s10973-020-09321-7.

33. Xue J, Grift TE, Hansen AC. Effect of biodiesel on engine performances and emissions. Renew Sustain Energy Rev [Internet]. Elsevier Ltd; 2011;15:1098–116. Available from: http://dx.doi.org/https://doi.org/10.1016/j.rser.2010.11.016.

34. Abdelmalek Z, Alamian R, Safdari Shadloo M, Maleki A, Karimipour A. Numerical study on the performance of a homogeneous charge compression ignition engine fueled with different blends of biodiesel. J Therm Anal Calorim [Internet]. Springer International Publishing; 2020; Available from: https://doi.org/10.1007/s10973-020-09513-1.

35. Abdul M, Jon HVG. The effect of biodiesel oxidation on engine performance and emissions. Biomass Bioenergy. 1998;20:213.

36. Namar MM, Jahanian O. Energy and exergy analysis of a hydrogen-fueled HCCI engine. J Therm Anal Calorim [Internet]. Springer International Publishing; 2019;137:205–15. Available from: https://doi.org/10.1007/s10973-018-7910-7.

37. He C, Ge Y, Tan J, You K, Han X, Wang J. Characteristics of polycyclic aromatic hydrocarbons emissions of diesel engine fueled with biodiesel and diesel. Fuel [Internet]. Elsevier Ltd; 2010;89:2040–6. Available from: https://doi.org/10.1016/j.fuel.2010.03.014.

38. Dolak J, Reitz RD. Optimization of the piston geometry of a diesel engine using a two-spray-angle nozzle. Proc Inst Mech Eng Part D J Automob Eng. 2011;225:406–21.

39. Jaichandar S, Senthil Kumar P, Annamalai K. Combined effect of injection timing and combustion chamber geometry on the performance of a biodiesel fueled diesel engine. Energy [Internet]. Elsevier Ltd; 2012;47:388–94. Available from: https://doi.org/10.1016/j.energy.2012.09.059.